Chemical Engineering Journal 428 (2022) 130771

Contents lists available at ScienceDirect

Chemical Engineering Journal

journal homepage: www.elsevier.com/locate/cej

Load-flexible fixed-bed reactors by multi-period design optimization

Ronny Tobias Zimmermann [a], Jens Bremer [b], Kai Sundmacher [a,b,*]

[a] Otto von Guericke University, Universitätsplatz 2, Chair for Process Systems Engineering, 39106 Magdeburg, Germany
[b] Max Planck Institute for Dynamics of Complex Technical Systems, Dpt. Process Systems Engineering, Sandtorstraße 1, 39106 Magdeburg, Germany

ARTICLE INFO

Keywords:
Load-flexible fixed-bed reactor
Power-to-methane
Multi-period design optimization
Dynamic reactor simulation

ABSTRACT

Many research activities focus on load-flexible fixed-bed reactors in the context of Power-to-X concepts. One of the main issues is the occurrence of hazardous temperature excursions in steady state and during dynamic load changes. The dilution of the catalytically active fixed-bed with inert particles and the use of catalyst particles with active core and inert shell (so-called core–shell catalyst particles) are proven means to prevent insufficient thermal management. This work aims at comparing both concepts with respect to the reactor's load-flexibility, exemplified for carbon dioxide methanation. In extension to our previous work of Zimmermann et al. (2020), a multi-period design optimization approach is performed for both concepts, considering one, two, and infinitely many axial fixed-bed segments. This approach simultaneously determines the optimal reactor design and operating parameters, which is inevitable for a sound technological comparison of the two concepts. Additionally, step responses are simulated as worst-case load change policy to switch from one optimized steady state to another. The results show that with core–shell particles shorter tubes can be used than with diluted fixed-beds, if one or two fixed-bed segments are considered. This results in lower pressure loss and higher space–time yield. Additionally, faster load changes can be realized with core–shell catalyst particles. In the case of infinitely many axial fixed-bed segments, both concepts converge to similar space–time yields, but show excessive temperature excursion during load changes.

1. Introduction

Due to the volatile availability of wind and solar energy, the current shift from nuclear and fossil fuels towards renewable energy sources will cause periods of energy surplus and shortage. A possibility to compensate for these fluctuations is energy storage via the synthesis of chemical compounds. This is known as Power-to-X concept, where 'X' is, for example, methane. In this context, hydrogen is produced by water electrolysis with surplus energy. Due to the lack of a hydrogen infrastructure and low energy density, hydrogen is subsequently converted with carbon dioxide, e.g., from technical waste streams, into methane (Synthetic Natural Gas) and fed into the natural gas grid. In this way, greenhouse gas emissions are also reduced. The exothermic methanation reaction is catalyzed by various metals. Nickel on alumina support is often a preferred, low-cost catalyst material, as it shows high activity and high methane selectivity [1].

$$CO_2 + 4H_2 \xrightleftharpoons{\text{e.g. } Ni/Al_2O_3} CH_4 + 2H_2O \quad H_r^0 = -164.9\ \frac{kJ}{mol}$$

Wall-cooled fixed-bed reactors are commonly used in the chemical industry to carry out highly exothermic heterogeneously catalyzed gas-phase reactions. However, due to the present market situation, the financial incentive to operate carbon dioxide methanation plants is currently low. In fact, the state-of-the-art is to produce hydrogen from fossil natural gas. As fixed-bed reactors are a central part of many methanation plant concepts, intensive research is being conducted into possible measures to improve reactor performance and safety. A central safety aspect in the operation of fixed-bed reactors is the avoidance of thermal runaway conditions, which occur if the released reaction heat exceeds the reactor's cooling capacity. This can lead to a significant temperature increase within the fixed-bed, damaging the catalyst and reactor material. The understanding and technical handling of this aspect has been the focus of research for several decades [2] and has gained new interest in the light of flexible reactor operation. This interest originates from an increased relevance of intermittent reactant supply (i.e., hydrogen) due to an upstream integration of renewable energy. Consequently, reactors must operate at various steady states and not, as usual, at a single steady state [3,4]. This demands all safety-related and economic process constraints to be met under all stationary conditions and during the transition in between.

Due to the non-linear dependence of the reaction rate on temperature, the limitation of the temperature-increase in fixed-bed reactors is a non-trivial task. Thus, different design and operation strategies

* Corresponding author.
E-mail address: sundmacher@mpi-magdeburg.mpg.de (K. Sundmacher).

https://doi.org/10.1016/j.cej.2021.130771
Received 13 January 2021; Received in revised form 31 May 2021; Accepted 5 June 2021
Available online 10 June 2021

have been investigated with focus on CO and CO_2 methanation. An established approach to limit the fixed-bed temperature increase is the dilution of reactants via product recycle [5–7]. While absorbing a fraction of the reaction heat, the product gas also shifts the chemical equilibrium of the methanation reaction towards the side of the reactants, and thus additionally decreases the rate of reaction heat release. Besides, other fixed-bed reactor concepts were investigated. Examples include the use of multiple cooling zones [8], multiple adiabatic reactors in series with intermediate cooling [9], structured reactors [10,11], membrane reactors [12] or intermediate feed gas injection/product removal [5,13]. The operation of polytropic fixed-bed reactors on unstable-operation points was investigated by Bremer and Sundmacher [14].

A further well-accepted and industrially applied approach to limit the upper reactor temperature and to avoid runaway conditions is to dilute the catalyst bed with an inert material [15,16]. As shown in the Arrhenius plot in Fig. 1, this procedure decreases the reaction rate and, thus, the heat release rate in the reactor. In consequence, the temperature in the reactor drops, and the reactor operation becomes safe. Luyben [17] also points out that the dynamic controllability of fixed-bed reactors with diluted fixed-bed is improved. However, this also leads to a drop in the reactor's space–time yield. For this reason, two or more segments of different dilution ratios are often used, which cause characteristic temperature profiles with multiple hot-spots and complex dynamic behavior [18–20]. Fischer and Freund [21] developed a methodology to include the dynamics of fixed-bed reactors into the design problem and applied it to design load-flexible fixed-bed tubular reactors [22]. Among others, the influence of multiple segments with different fixed-bed dilution ratios was investigated.

Besides fixed-bed dilution, some studies mention that the prevention of runaway conditions is also possible by an inert shell covering the active catalyst particles [23,24]. In the context of this study, such particles are called core–shell catalyst particles. If properly designed, the inert shell can significantly limit the effective reaction rate selectively at high temperatures, where the diffusion through the inert layer becomes rate-determining. On the other hand, if the layer thickness is sufficiently small, the effective reaction rate is hardly affected at low temperatures. In this domain, the reaction rate of the core is rate-determining, as seen in Fig. 1. Core–shell catalyst particles were identified as the best-possible catalyst particle design for load-flexible carbon dioxide methanation in our previous work [25]. The result is obtained by optimization of catalyst particle properties in a reactor with fixed geometry and constant operating variables, which is supplemented with sensitivity analyses and dynamic simulations.

Based on this result, we extend the procedure by considering multiple steady states with different loads in parallel in a single optimization of the whole catalyst-reactor system. Thus, optimal design and operating parameters for a load-flexible fixed-bed reactor are determined simultaneously. The focus is in particular on the comparison of fixed-bed dilution with inert material and the use of core–shell catalyst particles, as both concepts evolve very different trends on the catalyst level, which ultimately also affects the performance on the reactor level. The reactor performance measures to which this work primarily refers are space–time yield, safety, and flexibility. At first, optimal operation and design parameters are obtained by rigorously optimizing the methane space–time yield for both concepts considering one, two, and infinitely many fixed-bed segments for a single steady state. Each segment of the fixed-bed can consist of different catalyst loadings. Subsequently, the optimization of a single steady state is extended to a multi-period design optimization [26–28], to investigate the impact of alternating reactor loads on reactor design and operation. Finally, the transitions between the optimal steady-states are simulated to study transition times and behavior.

2. Model

The selection of a proper model is a crucial part of numerical studies and depends on the research question. Many fixed-bed reactor models with different degrees of accuracy and complexity have been developed over the years. Comparisons of some of these models in the framework of carbon dioxide methanation are given in [12,14,29]. Based on these results, a transient, one-dimensional description of the polytropic fixed-bed reactor is considered adequate for this work's aim. Together with proper correlations for reaction kinetics, heat transfer, and pressure drop, the model is able to reflect the behavior of more complex models (e.g. a two-dimensional, heterogeneous model) with sufficient accuracy. The computational effort to solve the model is comparatively low, which is necessary for a time-efficient and robust optimization approach.

The central element of the model are mass and energy balance equations for a single reactor tube, which is representative for the whole multi-tubular reactor. If a single reaction is considered, the mass balance equations of the components CO_2, H_2, CH_4 and H_2O can be unified in a single equation by using, for example, the carbon dioxide conversion X_{CO_2}:

$$\dot{n}_i = \dot{n}_{i,\mathrm{in}} + \nu_i \, X_{\mathrm{CO_2}} \, \dot{n}_{\mathrm{CO_2,in}} \tag{1}$$

with $i \in \{CO_2, H_2, CH_4, H_2O\}$. For simplicity X_{CO_2} is further on denoted as X. Together with the energy balance in temperature form, the transient balance equations of the reactor together with initial and boundary conditions read as:

$$\varepsilon_R \frac{\partial X}{\partial t} = -u \frac{\partial X}{\partial z} + \frac{M_{\mathrm{CO_2}}}{\rho \, y_{\mathrm{CO_2,in}}} \left(1 - \varepsilon_R\right) \zeta \, \sigma_{\mathrm{eff}}, \tag{2}$$

$$(\rho c_p)_{\mathrm{eff}} \frac{\partial T}{\partial t} = -u_{\mathrm{in}} \, \rho_{\mathrm{in}} c_p \frac{\partial T}{\partial z} + \frac{\partial}{\partial z}\left[\Lambda_{\mathrm{ax}} \frac{\partial T}{\partial z}\right] + \frac{4\,U}{D}\left(T - T_{\mathrm{cool}}\right) - H_{\mathrm{r}} \left(1 - \varepsilon_R\right) \zeta \, \sigma_{\mathrm{eff}}, \tag{3}$$

$$X|_{z=0} = 0, \qquad \Lambda_{\mathrm{ax}} \left.\frac{dT}{dz}\right|_{z=0} = u_{\mathrm{in}} \, \rho_{\mathrm{in}} \, c_p \, (T - T_{\mathrm{in}}), \qquad \left.\frac{\partial^2 T}{dz^2}\right|_{z=\mathfrak{L}} = 0, \tag{4}$$

$$X|_{t=0} = X_0, \qquad T|_{t=0} = T_0. \tag{5}$$

The axial dispersion of mass is neglected, as it is dominated by convective mass transport on the reactor scale. In steady-state, the axial dispersion of energy was found also to be negligible for all cases considered in this work. However, studies show that it can lead to a qualitatively different transient behavior, in comparison to a model, which ignores it [30–32]. Consequently, the axial energy dispersion is included in the model.

The energy balance's overall heat transfer coefficient U is expressed as a series of resistances consisting of the outer wall heat transfer coefficient, inner wall heat transfer coefficient, and the fixed-bed heat transfer resistance. It is calculated according to Dixon [33]

$$\frac{1}{U} = \frac{1}{\alpha_{\mathrm{w}}} + \frac{D}{6\,\Lambda_{\mathrm{r}}} \frac{\mathrm{Bi_w} + 3}{\mathrm{Bi_w} + 4}, \tag{6}$$

$$\text{with} \qquad \frac{1}{\alpha_{\mathrm{w}}} = \frac{1}{\alpha_{\mathrm{w,out}}} + \frac{1}{\alpha_{\mathrm{w,in}}}, \qquad \mathrm{Bi_w} = \frac{\alpha_{\mathrm{w}} \, D}{2\,\Lambda_{\mathrm{r}}}. \tag{7}$$

The effective axial and radial heat conductivity Λ_{ax} and Λ_{r} are determined by the equation of Yagi and Kunii [34]

$$\Lambda_{\mathrm{ax}} = \lambda_{\mathrm{bed}} + \frac{\mathrm{Pe}}{K_{\mathrm{ax}}} \lambda_{\mathrm{fluid}}, \qquad \Lambda_{\mathrm{r}} = \lambda_{\mathrm{bed}} + \frac{\mathrm{Pe}}{K_r} \lambda_{\mathrm{fluid}} \tag{8}$$

$$\text{with} \qquad K_{\mathrm{ax}} = 2, \qquad K_{\mathrm{r}} = 7\left[2 - \left(1 - \frac{2}{D/d}\right)^2\right], \qquad \mathrm{Pe} = \frac{u \, \rho \, c_p \, d}{\lambda_{\mathrm{fluid}}} \tag{9}$$

and $\alpha_{\mathrm{w,in}}$ according to the correlation of Martin and Nilles [35]. The required heat conductivity of the fixed-bed without fluid flow λ_{bed} is calculated according to the Zehner–Bauer–Schlünder model [36], which is discussed in detail in the VDI heat atlas [37]. The respective

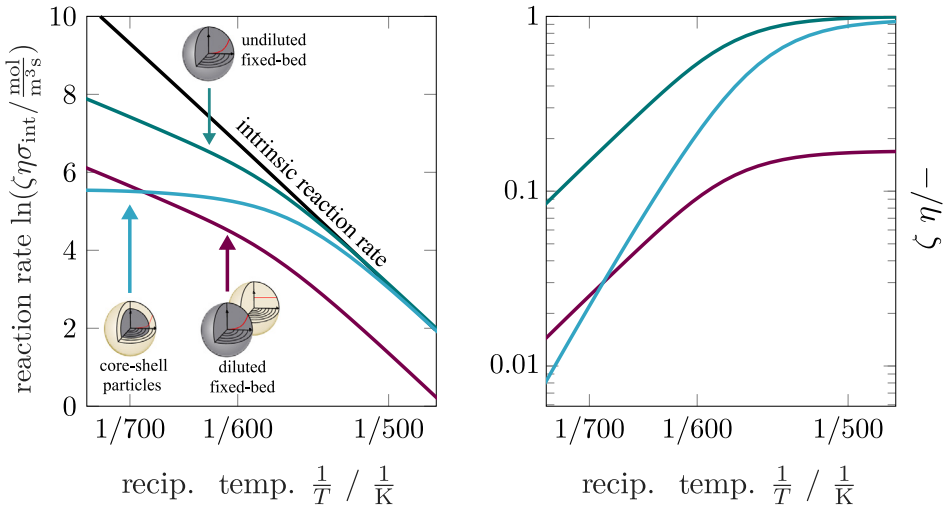

Fig. 1. Influence of fixed-bed dilution and an inert shell on the effective reaction rate displayed in Arrhenius plots (left side) as well as the product of the dilution ratio and effectiveness factor (right side). Additionally, the values of an undiluted fixed-bed ($\zeta = 1$) are shown. Curves calculated according to $\sigma = \zeta\,\eta\,\sigma_{\mathrm{int}}$ based on results given in Section 5 at $X_{\mathrm{CO_2}} = 0\%$.

equations are summarized in [25]. An approximation for the temperature in the center of the fixed-bed is also given by Dixon [33]:

$$T_{\mathrm{c}}(z) = \frac{U}{U'}\left(T - T_{\mathrm{cool}}\right) + T_{\mathrm{cool}},$$
$$U' = \alpha_{\mathrm{w}}\frac{\mathrm{Bi}_{\mathrm{w}}^4 + 24\,\mathrm{Bi}_{\mathrm{w}}^3 + 240\,\mathrm{Bi}_{\mathrm{w}}^2 + 1152\,\mathrm{Bi}_{\mathrm{w}} + 2304}{16\,\left(\mathrm{Bi}_{\mathrm{w}}^2 + 6\,\mathrm{Bi}_{\mathrm{w}} + 12\right)^2}. \tag{10}$$

The approximation was derived at steady-state conditions. Consequently, by applying this equation, it is assumed that the radial temperature profile is quasi-stationary. Quasi-stationarity is also assumed for the velocity and pressure profiles, which are calculated by the overall mass balance equation and the correlation of Eisfeld and Schnitzlein [38], respectively. As the pressure loss is often not a major factor in changing the reaction rate, it is assumed constant over the fixed-bed's length and is calculated at the inlet of the reactor.

$$u(z) = \frac{u_{\mathrm{in}}\,\rho_{\mathrm{in}}}{\rho(z)}, \tag{11}$$

$$p(z) = p_{\mathrm{in}} - \left[154\,A_{\mathrm{w}}^2\,\frac{(1-\varepsilon_R)^2}{\varepsilon_R^3}\,\frac{\mu_G\,u_{\mathrm{in}}}{d^2} + \frac{A_{\mathrm{w}}}{B_{\mathrm{w}}}\,\frac{1-\varepsilon_R}{\varepsilon_R^3}\,\frac{\rho_{\mathrm{in}}\,u_{\mathrm{in}}^2}{d}\right] z, \tag{12}$$

$$\text{with}\qquad A_{\mathrm{w}} = 1 + \frac{2}{3\,(D/d)\,(1-\varepsilon_R)},\qquad B_{\mathrm{w}} = \left[1.15\left(\frac{d}{D}\right)^2 + 0.87\right]^2. \tag{13}$$

Gas-phase properties are calculated as described in [25] with pure component data given in the VDI heat atlas [37] and the mixing rules described by Poling et al. [39].

The intrinsic reaction rate of the catalyst particles is given by Koschany et al. [40]. It was determined on a Ni/Al(O)$_x$ catalyst. The model is valid for temperatures from 453 to 613 K and pressures from 1 to 15 bar.

$$\sigma_{\mathrm{int}} = \frac{k\,p_{\mathrm{CO_2}}^{0.5}\,p_{\mathrm{H_2}}^{0.5}\left(1 - \frac{p_{\mathrm{CH_4}}\,p_{\mathrm{H_2O}}^2}{K_{\mathrm{eq}}\,p_{\mathrm{CO_2}}\,p_{\mathrm{H_2}}^4}\right)}{\left(1 + K_{\mathrm{OH}}\,\frac{p_{\mathrm{H_2O}}}{p_{\mathrm{H_2}}^{0.5}} + K_{\mathrm{H_2}}\,p_{\mathrm{H_2}}^{0.5} + K_{\mathrm{mix}}\,p_{\mathrm{CO_2}}^{0.5}\right)^2} \tag{14}$$

The model is extrapolated for this study. This has to be considered when interpreting the results because the occurrence of side reactions (e.g., reverse water gas shift reaction) is neglected. However, the quantities of side products produced are comparably small, as shown in Appendix A. Thus, the general behavior of the fixed-bed reactor remains the same [41].

As part of this study is to investigate the influence of an inert shell on catalyst particles, mass transport limitations at the catalyst particle scale have to be considered. This is done by multiplying the catalyst effectiveness factor with the intrinsic reaction rate to get the effective reaction rate according to

$$\sigma_{\mathrm{eff}} = \eta\,\sigma_{\mathrm{int}} = \frac{\sigma_{\mathrm{int}}}{(1+\delta)^{n+1}\left[\frac{\Phi}{\tanh(\Phi)} + \frac{\Phi^2}{\mathrm{Bi_{ext}}\,(1+\delta)^n} + \frac{\Phi^2}{\mathrm{Bi_{int}}}\right]}, \tag{15}$$

with

$$\Phi = \frac{R_{\mathrm{core}}}{n+1}\sqrt{\frac{\sigma_{\mathrm{int}}(c_{\mathrm{bulk}})}{\mathfrak{D}_{\mathrm{core}}\,(c_{\mathrm{bulk}} - c_{\mathrm{bulk,eq}})}},\qquad \mathrm{Bi_{ext}} = \frac{\beta_{\mathrm{CO_2}}\,R_{\mathrm{core}}}{\mathfrak{D}_{\mathrm{core}}(n+1)},$$
$$\mathrm{Bi_{int}} = \frac{\mathfrak{D}_{\mathrm{shell}}}{\mathfrak{D}_{\mathrm{core}}\,R_{\mathrm{core}}^{n-1}\,\Psi(n+1)},\qquad \delta = \frac{R_{\mathrm{shell}} - R_{\mathrm{core}}}{R_{\mathrm{core}}}.$$

A detailed derivation of Eq. (15) and a comparison to a rigorously solved catalyst particle model is given in Appendix B. The effective diffusion coefficients, heat conductivities and mass transfer coefficient are calculated by [42,43]

$$\mathfrak{D}_{\mathrm{core/shell}} = \frac{\varepsilon_{\mathrm{core/shell}}}{\tau_{\mathrm{core/shell}}}\,\frac{d_{\mathrm{pore,core/shell}}}{3}\sqrt{\frac{8}{\pi}\,\frac{R_{\mathrm{gas}}\,T}{M_{\mathrm{CO_2}}}}, \tag{16}$$

$$\lambda_{\mathrm{core/shell}} = \frac{1-\varepsilon_{\mathrm{core/shell}}}{\tau_{\mathrm{core/shell}}}\,\lambda_{\mathrm{solid,core/shell}}, \tag{17}$$

$$\beta_{\mathrm{CO_2}} = \frac{\mathfrak{D}_{\mathrm{M,CO_2}}}{d}\left(2 + 1.1\left(\frac{\mu_G}{\rho_G\,\mathfrak{D}_{\mathrm{M,CO_2}}}\right)^{1/3}\left(\frac{u\,\rho_G\,d}{\mu_G}\right)^{0.6}\right). \tag{18}$$

Methanation catalysts are usually mesoporous with pore diameters in the range from 5 to 20 nm. Thus, Knudsen diffusion is assumed to be the primary mechanism of mass transport within the catalyst particles. For estimating the tortuosity of the catalyst particles, the Bruggeman relationship $\tau = \varepsilon^{0.5}$ is used [44]. Based on former studies, the catalyst particles are assumed isothermal [12,25]. However, the heat conductivity is required for calculating the effective axial and radial heat conductivity coefficients at the reactor scale. As the catalyst particle core and shell heat conductivity can differ, they are averaged according to the coated sphere model [45]:

$$\lambda_{\mathrm{cat}} = \lambda_{\mathrm{core}}\left[1 + (\gamma-1)\,\Theta - \frac{(\gamma-1)^2\,\Theta\,(1-\Theta)}{3\,\gamma + (\gamma-1)\,\Theta}\right], \tag{19}$$

$$\gamma = \frac{\lambda_{\mathrm{shell}}}{\lambda_{\mathrm{core}}} > 1,\qquad \Theta = \frac{r_{\mathrm{shell}}^3 - r_{\mathrm{core}}^3}{r_{\mathrm{shell}}^3}. \tag{20}$$

Table 1
Degrees of freedom DoF depending on the reactor design concept.

case 1a	Uniformly diluted fixed-bed	ζ
case 2a	Uniform fixed–bed of core–shell catalyst particles	$\delta, \epsilon_{\text{shell}}, d_{\text{pore,shell}}$
case 1b	Two segments of different dilution ratios	$\zeta_1, \zeta_2, z_{\text{switch}}$
case 2b	Two segments of different shell thickness	$\delta_1, \delta_2, z_{\text{switch}}, \epsilon_{\text{shell}}, d_{\text{pore,shell}}$
case 1c	Dilution ratio variable along the fixed–bed	$\zeta(z)$
case 2c	Shell thickness variable along the fixed–bed	$\delta(z), \epsilon_{\text{shell}}, d_{\text{pore,shell}}$
All cases		$N_T, \mathfrak{L}, D, r_{\text{core}}, T_{j,\text{in}}, u_{j,\text{in}}, p_{j,\text{in}}, T_{j,\text{cool}}, \alpha_{j,\text{out}}$

3. Optimization problem

This work aims to design a multi-tubular fixed-bed reactor, which is able to convert a carbon dioxide stream into Synthetic Natural Gas (SNG) in an optimal manner. For this purpose, carbon dioxide is mixed with hydrogen in stoichiometric ratio ($\dot{n}_{\text{H}_2}/\dot{n}_{\text{CO}_2} = 4/1$) and fed to the multi-tubular reactor. The supplied hydrogen stems from an electrolysis unit powered by an alternating supply of renewable energy. Thus, hydrogen generation is not constant and the fixed-bed methanation reactor has to operate flexibly depending on the installed buffer units. We assume that N reactor loads are equally likely and uniformly spaced with a mean of $\bar{L}_{\text{CO}_2}$ and load range $\Delta L_{\text{CO}_2} = L_{\text{CO}_2,\text{max}} - L_{\text{CO2,min}}$.

$$L_{\text{CO}_2,j} = \bar{L}_{\text{CO}_2} + \left(j - \frac{N+1}{2}\right)\frac{\Delta L_{\text{CO}_2}}{N-1} \qquad \text{for } j \in \{1,\dots,N\} \tag{21}$$

For every possible load, economic and safety requirements have to be met. In our case, this translates to requirements for $T_c \leq 750\,\text{K}$ and $X(\mathfrak{L}) \geq 95\%$. We assume that if these conditions are not met, the catalyst deactivates or the SNG post-treatment costs become uneconomically high, respectively. A further important fixed-bed reactor design aspect is pressure loss, which is reflected in the required compression power and therefore in plant operating costs. However, since these depend on the design of the plant, the pressure loss is left unconstrained in this study.

To avoid an infeasible operation, the design and operating parameters have to be chosen accordingly. The design parameters have technological bounds and are the same for each load, such as the reactor tube number, diameter, and length. The operating parameters can be varied according to the load, such as inlet pressure, inlet velocity, inlet temperature, coolant temperature, and the outer wall heat transfer coefficient.

Further design parameters are obtained depending on the reactor design concept. In the case of fixed-bed dilution (denoted *case 1*), this is the dilution ratio $\zeta = V_{\text{cat}}/(V_{\text{cat}} + V_{\text{inert}})$, which is multiplied with the source term in balance Eqs. (2) and (3). Although the inert dilution material can have different properties than the catalyst, such as heat conductivity or particle diameter, we assume these properties to be the same. In reactor designs with core–shell particles (denoted *case 2*), pore diameter, porosity, and shell thickness can be chosen within specified bounds (see Tables 1 and 2).

As discussed in the introduction, multiple segments with different catalyst bed compositions can be used. Therefore, *case 1* and *2* are further distinguished in three sub-cases. In *Sub-case a*, the catalyst bed is uniform within the whole reactor. In *Sub-case b*, two consecutive beds of different compositions can be used. The two beds differ either by the fraction of inert material (*case 1b*) or by the thickness of the inert shell (*case 2b*). A switch function gives the spatial distribution of the respective parameter:

$$\xi(z) = (\xi_2 - \xi_1)\left[0.5 + \frac{0.5(z - z_{\text{switch}})}{\sqrt{(z - z_{\text{switch}})^2 + \kappa}}\right] + \xi_1, \tag{22}$$

where $\xi \in \{\zeta, \delta\}$ is the switched parameter, z_{switch} is the switching position and κ, which equals 10^{-4} in this study, determines the sharpness of the transition. In *Sub-case c*, the dilution ratio and the shell thickness can be varied freely along the reactor's length.

Table 2
Optimization constraints, variables, parameters, and bounds for loads $j \in \{1,..,N\}$ [12,41,46–48].

Technological constraints	
Conversion bounds	$X_j(\mathfrak{L}) \geq 95\%$
Temperature bounds	$T_{j,c} \leq 750\ \text{K}$
Tube/particle diameter ratio	$D/d \geq 8$
Inlet temperature constraint	$T_{j,\text{in}} \geq T_{j,\text{cool}}$
Load constraint	$L_{\text{CO}_2,j} = N_T\ \frac{\pi}{4}\ D^2\ u_{j,\text{in}}\ \rho_{j,\text{in}}\ y_{\text{CO}_2,\text{in}}$
Operating parameter constraints	
Inlet pressure	$2\ \text{bar} \leq p_{j,\text{in}} \leq 20\ \text{bar}$
Inlet velocity	$0.1\ \text{m/s} \leq u_{j,\text{in}} \leq 1.5\ \text{m/s}$
Inlet temperature	$500\ \text{K} \leq T_{j,\text{in}} \leq 750\ \text{K}$
Coolant temperature	$500\ \text{K} \leq T_{j,\text{cool}} \leq 750\ \text{K}$
Outer wall heat transfer coefficient	$250\ \text{W/(m}^2\ \text{K)} \leq \alpha_{j,\text{out}} \leq 2000\ \text{W/(m}^2\ \text{K)}$
Flow constraints	Eq. (21)
Design parameter constraints	
Number of tubes	$1 \leq N_T \leq 10\,000$
Tube length	$0.1\ \text{m} \leq \mathfrak{L} \leq 20\ \text{m}$
Tube diameter	$2\ \text{cm} \leq D \leq 5\ \text{cm}$
Particle core radius	$1\ \text{mm} \leq r_{\text{core}} \leq 2.5\ \text{mm}$
Particle shell radius	$1\ \text{mm} \leq r_{\text{shell}} \leq 2.5\ \text{mm}$
Particle shell porosity	$0.1 \leq \epsilon_{\text{shell}} \leq 0.7$
Particle shell pore diameter	$5\ \text{nm} \leq d_{\text{pore,shell}} \leq 25\ \text{nm}$
Catalyst particle fraction	$\zeta = 100\%$ (catalyst with inert shell) $0\% \leq \zeta \leq 100\%$ (fixed-bed dilution)
Particle shell constraint	$r_{\text{core}} \leq r_{\text{shell}}$ (catalyst with inert shell) $r_{\text{core}} = r_{\text{shell}}$ (fixed-bed dilution)
Switching position (for *case 1b* and *case 2b*)	$0 \leq z_{\text{switch}} \leq \mathfrak{L}$
Fixed parameters	
Core porosity	$\epsilon_{\text{core}} = 0.5$
Core pore diameter	$d_{\text{pore,core}} = 10\ \text{nm}$
Core solid density	$\rho_{\text{solid,core}} = 3000\ \text{kg/(m}^3\text{)}$
Shell solid density	$\rho_{\text{solid,shell}} = 3000\ \text{kg/(m}^3\text{)}$
Core solid heat conductivity	$\lambda_{\text{solid,core}} = 1\ \text{W/(m K)}$
Shell solid heat conductivity	$\lambda_{\text{solid,shell}} = 1\ \text{W/(m K)}$
Core solid heat capacity	$c_{p,\text{solid,core}} = 1000\ \text{J/(kg K)}$
Shell solid heat capacity	$c_{p,\text{solid,shell}} = 1000\ \text{J/(kg K)}$
Carbon dioxide inlet mass fraction	$y_{\text{CO}_2,\text{in}} = 0.846$
Hydrogen inlet mass fraction	$y_{\text{H}_2,\text{in}} = 0.154$

For each case, numerical optimization is performed to maximize the mean methane space–time yield over all loads

$$\overline{STY}_{\text{CH}_4} = \frac{\sum_{j=1}^{N} STY_{\text{CH}_4,j}}{N}. \tag{23}$$

In summary, the general formulation of the resulting nonlinear optimization problem is given by

$$\begin{aligned} \max_{DoF} \quad & \overline{STY}_{\text{CH}_4}(\bar{L}_{\text{CO}_2}, \Delta L_{\text{CO}_2}, N, \text{case}) \\ \text{s.t.} \quad & \text{reactor model Eqs. (1) to (20)} \\ & \text{technological constraints (Table 2)} \\ & \text{operating constraints (Table 2)} \\ & \text{design constraints (Table 2)} \end{aligned}$$

with the degrees of freedom DoF given in Table 1.

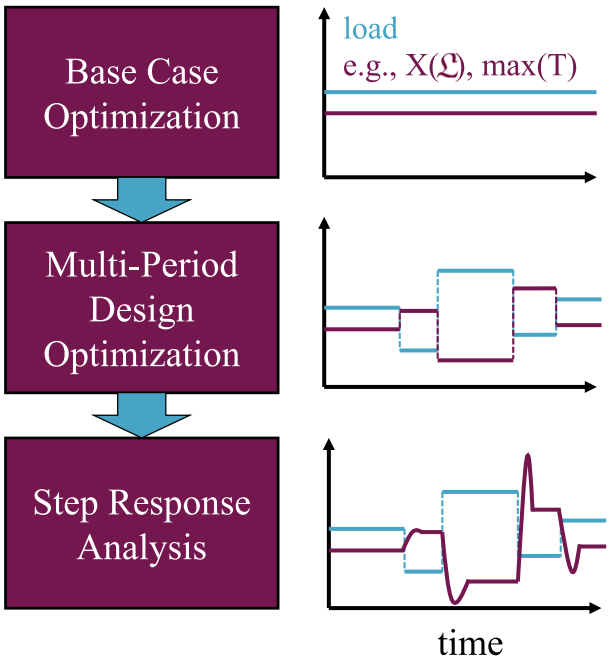

Fig. 2. Schematic representation of the solution methodology.

4. Solution methodology and computational aspects

As shown in Fig. 2, the results of this study are obtained in three steps. At first, the optimization problems are solved with a constant load ($\bar{L}_{CO_2} = 1$ t/h, $\Delta L = 0$ t/h). This is called *base case* optimization. The optimal design and operating parameters are discussed, and the performance of all reactor concepts is compared.

Subsequently, the influence of a predetermined load range on the optimal choice of design and operating parameters (also called design and control variables) is investigated by performing multi-period design optimizations [26–28] for each case displayed in Table 1. In the performed multi-period design optimizations, the reactor is subject to N piecewise constant loads in successive periods. The steady states are assumed to be much longer than the transitions in between and thus the reactor dynamics are neglected. This also implies that the order of the periods has no influence on the result. The operating parameters are optimally adjusted within their specified bounds for each period individually. As the optimal design parameters cannot be changed during reactor operation, their optimal values are determined by all loads simultaneously. In total, 15 loads ($N = 15$), which are distributed according to Eq. (21) are considered in each multi-period design optimization. An individual multi-period design optimization for various load ranges from 0 t/h (constant load) to 1 t/h (changing load) is performed. During all studies, the mean carbon dioxide load is kept constant at 1 t/h.

After successful optimization, all constraints are fulfilled for each steady state. However, during a dynamic transition from one steady state to another, some constraints might be violated. Therefore, step responses of the reactor upon changes of load and operating parameters are examined as worst–case load-change policy. In this way, unfavorable behavior on sudden load changes, such as temperature overshoots and conversion drops, can be detected. Furthermore, this procedure gives insight into the time-scale of load-changes, which allows to judge whether the steady-state assumption of the multi-period design optimization is assessable.

To apply the discussed methodology, the balance equations (Eqs. (2) and (3)) are discretized into 300 control volumes by the Finite Volume Method. The control volumes are logarithmically spaced along the reactor's axis, with smaller control volumes at the inlet of the reactor, where steeper profiles are expected. The resulting equations are implemented into MATLAB2016a within the CasADi framework [49, 50]. Based on the information given in [25], an initial guess on the optimal parameters of the *base case* optimization is made. The system is integrated into steady state via the CVodes integrator of SUNDIALS [51]. The obtained solution is used for initialization of the *base case* optimization. Subsequently, the multi-period design optimizations are carried out by carefully increasing the load range. Each multi-period design optimization is initialized with the optimal solution of the previous. As optimization solver, Ipopt [52] with MA97 [53] as underlying linear solver is selected. The subsequent step response analyses are also performed by employing the CVodes integrator of SUNDIALS [51].

Table 3
Optimal base case parameters.

	Unit	case					
		1a	2a	1b	2b	1c	2c
Performance parameters							
Methane space–time yield	$\frac{kg_{CH_4}}{m^3\ s}$	0.17	0.57	0.96	1.11	1.26	1.31
Outlet conversion	%	95.0	95.0	95.0	95.0	95.0	95.0
Max. fixed-bed temp.	K	750	750	750	750	750	750
Pressure loss	bar	6.49	2.00	1.14	1.07	1.17	0.89
Optimal parameters							
Inlet temperature	K	574	569	584	557	562	566
Inlet velocity	$\frac{m}{s}$	1.50	1.50	1.50	1.50	1.50	1.50
Inlet pressure	bar	20.0	20.0	20.0	20.0	20.0	20.0
Coolant temperature	K	574	569	555	557	562	566
Outer wall heat trans. coeff.	$\frac{kW}{m^2\ K}$	2.00	2.00	2.00	2.00	2.00	2.00
Tube length	m	11.0	3.37	1.95	1.77	1.54	1.48
Tube diameter	cm	2.00	2.00	2.00	2.00	2.00	2.00
Number of tubes	–	160	158	162	155	157	158
Particle core radius	mm	1.25	1.23	1.25	1.00	1.00	1.00
Particle shell porosity	–	–	0.10	–	0.33	–	0.33
Particle shell pore diameter	nm	–	5.00	–	14.7	–	12.3

5. Results

5.1. Base case optimization

The *base case* optimization results are shown in Fig. 3 and Table 3. In all studies, the highest possible inlet pressure and inlet velocity are preferred, as this minimizes the required fixed-bed reactor cross-section. For each case, the fixed-bed reactor cross-section is divided into about 160 tubes with 2 cm diameter. Therefore, together with the outer wall heat transfer coefficient at the upper bound of 2000 W/(m^{2}K), the highest possible coolant heat transfer is selected. Inlet and coolant temperature are chosen in the range of 557–584 K. This temperature range enables to limit the hot-spot temperature to 750 K on the one hand, but allows for high reaction rates towards the reactor's outlet on the other hand. Consequently, the difference in methane space–time yields is mainly determined by the tube length necessary to achieve the required outlet conversion of 95%.

The lowest methane space–time yield is achieved with a single segment of diluted fixed-bed (*case 1a*), where the amount of catalyst is reduced to about 20%. As shown in Fig. 3, the fixed-bed dilution significantly reduces the effective reaction rate at high temperatures and, thus, allows to keep the hot-spot temperature in the limit of 750 K. However, as the fixed-bed dilution is constant over the fixed-bed's whole length, the effective reaction rate is also reduced towards the reactor's outlet, where the temperature is relatively low. In consequence, comparably long tubes of 11.0 m with a considerable pressure loss of 6.5 bar are necessary to achieve a conversion of 95%. As this result is obtained by numerical optimization, it is evident, that a fixed-bed methanation reactor cannot be operated at the given conditions with an undiluted fixed-bed of uniform catalyst particles. The reason for this is, that if an operation with an undiluted fixed-bed would be possible,

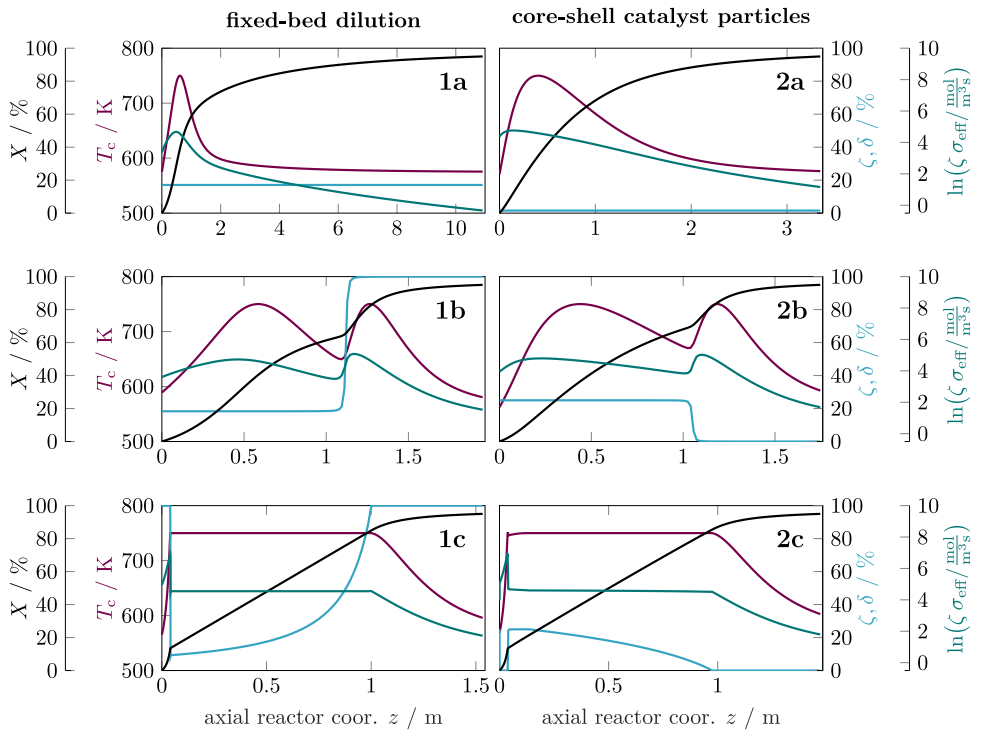

Fig. 3. Base case optimization results: Conversion, temperature, and effective reaction rate profiles together with either optimal fixed-bed dilution (left) or inert shell thickness (right) profiles.

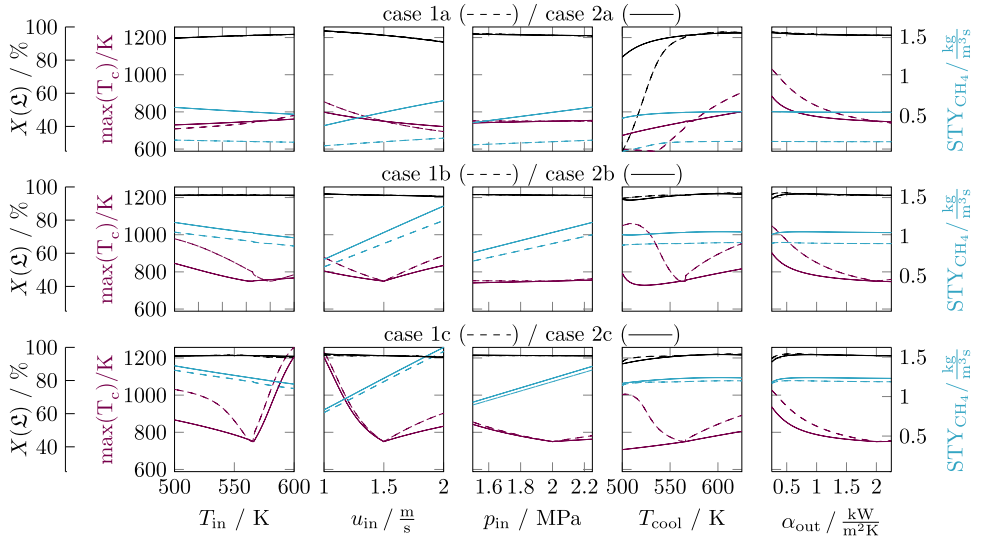

Fig. 4. Sensitivity analyses of carbon dioxide conversion, maximum fixed-bed temperature, and methane space–time yield depending on operating parameters. Dashed lines represent the reactor filled with diluted fixed-bed and solid lines the reactor filled with core–shell particles.

the optimization solver would prefer this option, as the inert material decreases the reactor space–time yield.

Higher space–time yields are possible by applying an inert shell onto the catalyst particles (*case 2a*). The inert shell's porosity and pore diameter are chosen such that the effective diffusion coefficient becomes minimal. This allows the shell to be as thin as possible for diffusion through the inert shell to become rate-determining at high temperatures and thus to limit the temperature to 750 K. On the other hand, the thin shell does not significantly influence the effective reaction rate towards the reactor's outlet, where no limitation of the effective reaction rate is necessary. Thus, a much shorter tube length compared to fixed-bed dilution is sufficient to achieve a conversion of 95%, which also results in a lower pressure loss of about 2 bar. As shown by the sensitivity analyses in Fig. 4, *case 2a* also reduces the parametric sensitivity of the reactor, especially concerning the outer wall heat transfer coefficient and the coolant temperature.

Significantly higher methane space–time yields are achieved when two segments of different catalyst loadings are introduced into the reactor (*case 1b* and *2b*). Both with fixed-bed dilution and inert shell, the second segment consists of a pure catalyst bed, which leads to the typical double-humped temperature profile. Since this procedure increases the amount of active catalyst and the reactor temperature, the average effective reaction rate also increases. Thus, much shorter tubes are sufficient to achieve the necessary outlet conversion of 95%. However, the increase in methane space–time yield is accompanied by a more complex reactor behavior, as shown by sensitivity analyses in

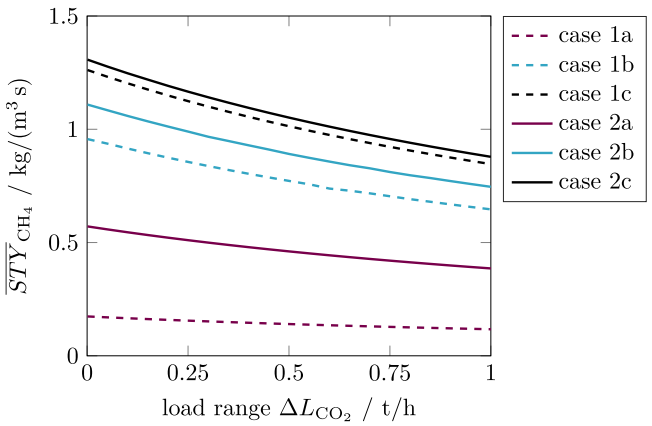

Fig. 5. Maximum mean methane space–time yield depending on the carbon dioxide load range.

Fig. 4. As discussed by Quina and Quinta Ferreira [19], either the first or the second hot spot can rise, depending on whether an operating parameter is increased or decreased. Consequently, the optimized points' temperature is minimal for all operating parameters, except for the pressure. Similar to *Sub-case a*, the two-segment reactor with optimal fixed-bed dilution (*case 1b*) is more sensitive to changes in operating parameters than the reactor with core–shell catalyst particles (*case 2b*).

Case 1c and *Case 2c* yield the upper bound of space–time yield achievable by both reactor concepts. For these cases, the reactors are filled with a short segment of pure, uniform catalyst particles close to the inlet, where the center temperature quickly rises to the upper bound. As soon as the upper temperature bound is attained, the fixed-bed is diluted or an inert shell is applied respectively to keep the temperature at the upper bound. Afterward, the fixed-bed dilution and the shell thickness decrease back to zero. This characteristic shape is known as a singular arc or singular segment in optimal control theory [16,18]. The obtained solutions show pronounced parametric sensitivity depending on the operating parameters, due to the segment with pure, uniform catalyst particles at the beginning of the reactors. The space–time yields for both concepts are almost the same. However, the reactor filled with core–shell catalyst particles performs slightly better. The reason is that the inert shell slightly increases the effective heat conductivity of the fixed-bed, as the optimally designed shell has a lower porosity than the porous cores. This allows for slightly higher effective reaction rates compared to the partially diluted catalyst bed, without surpassing the temperature limit. The effect, however, is minor.

5.2. Multi-period design optimization

Multi-period design optimizations for an increasing load range from 0 to 1 t/h were performed and the objective values are illustrated in Fig. 5, respectively. Note that the load range of 0 t/h corresponds to the *base case*, and all average space–time yields drop with increasing load range. The main reason for this drop is the increasing number of tubes, which rises linearly by 50% from about 160 to 240 in each case. This is in accordance with the increase in the maximum load from 1 t/h to 1.5 t/h. At the same time, the remaining design parameters remain identical to those of the *base case* shown in Table 3. In addition, the optimal operating parameters at the maximum load are the same as for the *base case*. Consequently, the optimizer favors a larger number of tubes over modifying the base case single tube design to handle the maximum reactor load. The additional tube volume is then redundant at lower reactor loads. Thus, the operating parameters are adjusted by the optimization such that the upper temperature limit is not exceeded while the conversion is kept above 95%. However, this offers little potential to compensate for the loss of methane space–time yield, as only a few percentage points are missing from total conversion, and the reaction is limited by thermodynamic equilibrium.

For a load range of 1 t/h, the optimal profiles of the operating parameters, together with the respective conversion and temperature profiles, are shown in Fig. 6 for fixed-bed dilution and Fig. 7 for the core–shell particle concept. The optimal inlet velocity and inlet pressure increase with increasing load, as long as neither parameter is at the upper bound. This is because higher pressures shift the hot-spot towards the reactor inlet, while higher velocities shift the hot-spot towards the reactor outlet. The influence of both parameters, therefore, compensates mutually. Except for *case 2b*, the inlet temperature is always determined by the coolant temperature due to the constraint $T_{in} \geq T_{cool}$. In general, the coolant temperature decreases with decreasing inlet velocity, to compensate for the decrease in the effective radial heat conductivity.

The reactors' temperature profile is also adjusted by changing the outer wall heat transfer coefficient, although for *case 1a* and *2a* it is optimal at its upper bound of 2 kW/(m^2 K) for all loads. For *case 1b* it exhibits a steep gradient and for *case 2b* even a discontinuity. For the remaining cases, it decreases monotonically with declining load. In all cases, the operating parameters are chosen such that the maximum temperature of 750 K is achieved at least at one point.

As frequent temperature changes of high magnitude could deactivate the catalyst, the maximum temperature difference ΔT_c is seen as an important characteristic feature for load flexible reactors. The maximum temperature difference in a single spot is 85.3 K for the diluted catalyst bed (*case 1a*) and 66.0 K for the core–shell particle concept (*case 2a*). For both cases, the hot-spot stays in a narrow section of about 25 cm near the reactor inlet.

For the reactors with two uniform fixed-bed segments (*case 1b* and *2b*), the double-humped temperature profile is maintained at all loads. However, the maximum temperature difference is 158.3 K for the diluted catalyst bed (*case 1b*) and only 77.1 K for the core–shell particle concept (*case 2b*). For the fixed-bed dilution case with infinite segments (*case 1c*), sagging temperature profiles are obtained with temperature maxima in the second half of the singular arc for loads lower than the maximum load. For the reactors filled with core–shell catalyst particles (*case 2c*), the temperature profiles have a maximum in the middle of the singular arc. Again, the maximum temperature difference for the reactor with core–shell particles ($\Delta T_c = 52.6$ K) is smaller than that of the reactor filled with a diluted catalyst bed ($\Delta T_c = 71.7$ K).

5.3. Step response analyses

Whereas all constraints are met in all optimized steady states, temperature excursions and conversion drops might still occur during the transition between each steady state, as shown in several works [21, 54]. Thus, the optimal operating parameter setting is switched between minimum, mean, and maximum load in terms of step changes, as shown in Fig. 8 (top). Each load is held for 5 min before another load change is applied.

For a uniform fixed-bed with core–shell particles (*case 2a*) the new steady-state settles much faster compared to a uniformly diluted fixed-bed (*case 1a*). Apart from temporally limited conversion undershoots during positive load changes, a minor oscillation of the temperature profile occurs before the new steady state stabilizes. This oscillation is much more pronounced for the reactor with a uniformly diluted fixed-bed (*case 1a*), especially after negative load changes.

Even more pronounced temperature excursions far above the tolerable temperature limit occur on negative load changes for reactors with two fixed-bed segments, of which the first is partially diluted with inert material (*case 1b*). In this case, the hot-spot in the diluted segment grows and travels in axial direction to the undiluted segment. As the hot-spot displacement is a comparably slow process, moving reaction fronts must be avoided if load flexibility is aspired. In this regard, the use of core–shell particles within the first segment (*case 2b*)

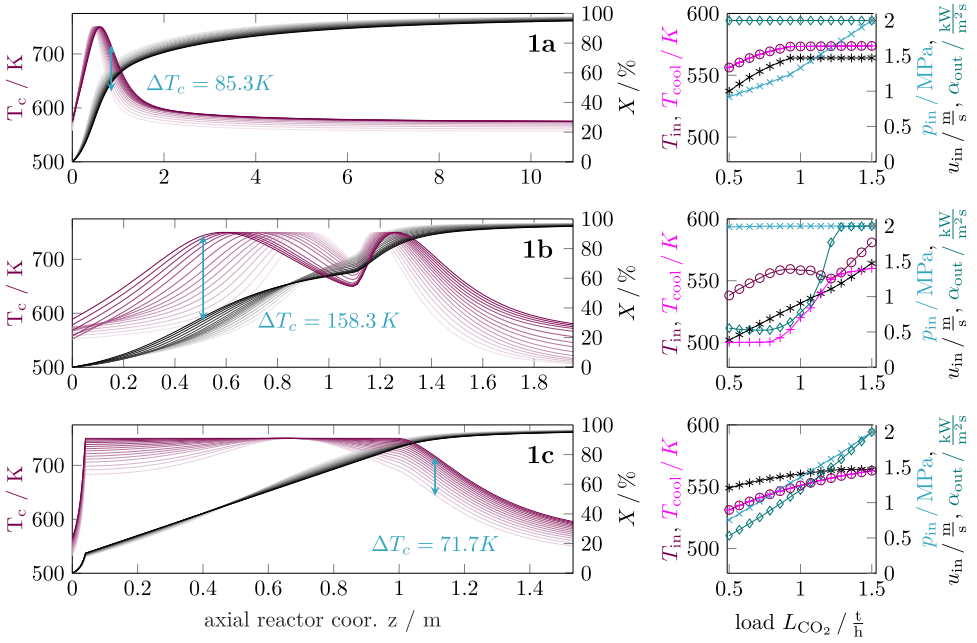

Fig. 6. Left: steady-state conversion and temperature profiles with optimal fixed-bed dilution for various loads with a carbon dioxide load range of 1 t/h. Darker colors belong to steady states with higher loads. Right: respective optimal operating parameters.

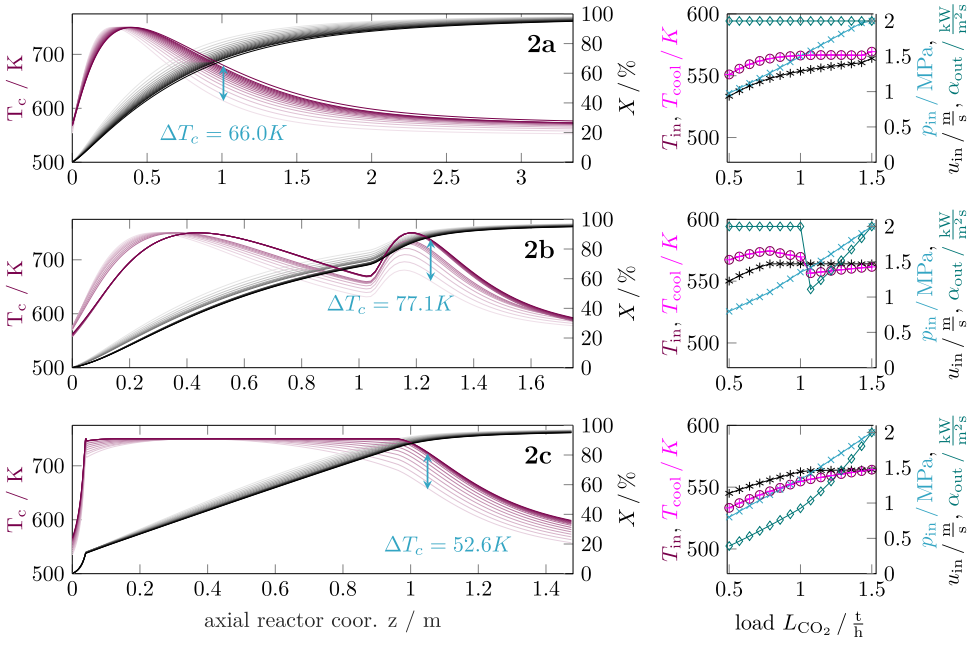

Fig. 7. Left: steady-state conversion and temperature profiles with optimal core–shell catalyst particles for various loads with a carbon dioxide load range of 1 t/h. Darker colors belong to steady states with higher loads. Right: respective optimal operating parameters.

is preferable, as traveling hot-spots and slow transitions are not an issue here.

For reactors with infinite fixed-bed segments (*case 1c* and *2c*), a significant temperature overshoot can be seen on negative load changes for both cases. The temperature overshoot begins in the inlet section with pure catalyst right before the singular arc. It then starts to travel towards the reactor outlet. With fixed-bed dilution (*case 1c*), the hot-spot travels a much larger distance, where the maximum of the temperature profile is located in the second half of the singular arc. In contrast, with core–shell catalyst particles (*case 2c*) the temperature overshoot quickly flattens and the new steady state is attained much faster compared to the reactor with a diluted catalyst bed.

6. Conclusion

The influence of fixed-bed dilution and the core–shell catalyst particle concept on steady-state and dynamic fixed-bed reactor operation have been compared in this work. Both concepts' specific features are free to choose within one, two, and infinitely many segments along the reactor axis. *Base case* design optimizations, multi-period design optimizations, and dynamic simulations between the optimal steady states are conducted to evaluate the performance of all cases with respect to space–time yield, maximum temperature, and load flexibility.

As other authors have already concluded, the steady-state performance of multi-tubular reactors with diluted fixed-bed increases with

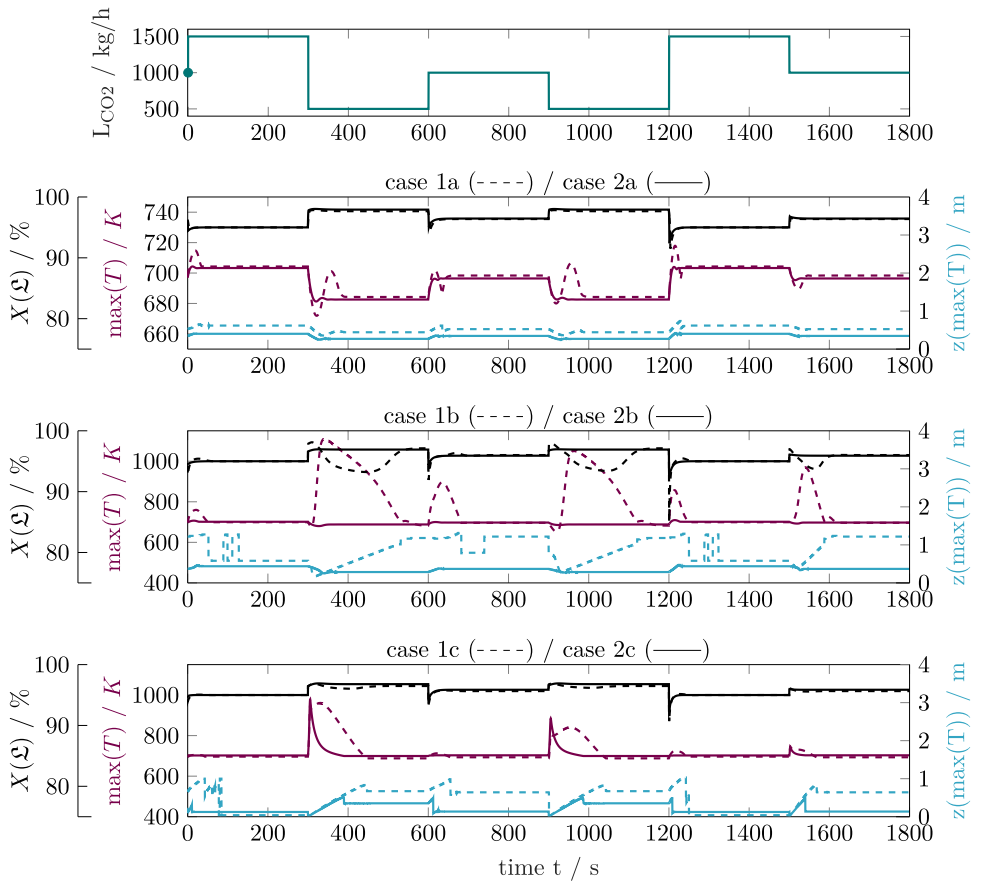

Fig. 8. Dynamic profiles of reactor load, outlet conversion, maximum (radially averaged) temperature and position thereof for multi-period optimized cases. (Instead of the fixed-bed center temperature T_c, the radially averaged temperature T is shown, as Eq. (10) is only valid in steady-state. Please also note the different temperature scales.)

an increasing number of optimally diluted fixed-bed segments [18]. This study shows that the same statement holds for reactors filled with catalyst particles consisting of an active core and an inert shell. The axial profile of the optimal shell thickness resembles the optimal dilution profile. However, especially if one or two fixed-bed segments are considered, the reactor filled with core–shell catalyst particles shows a significantly higher methane space–time yield, as shorter reactor tubes can be used compared to its counterpart with a diluted fixed-bed. This advantage results from a decrease of the effective reaction rate selectively at high temperatures, where the mass transport through the inert shell becomes rate-determining. Thus, the effective reaction rate becomes almost independent of temperature (and linear in concentration) since Knudsen diffusion is the major transport mechanism within the inert shell. In comparison, fixed-bed dilution decreases the effective reaction rate equally over the whole temperature range and does not change its dependence on temperature and concentration. A detailed sensitivity analysis reflects this fundamental difference between both concepts. The reactors filled with core–shell catalyst particles are much less sensitive towards changes in operating parameters, especially concerning the inlet and coolant temperature as well as the outer heat transfer coefficient. Additionally, due to the shorter tubes, the pressure loss of reactors filled with core–shell catalyst particles is lower than in the respective cases with diluted fixed-bed.

Multi-period design optimizations revealed that the mean space–time yield of all cases drops with an increasing load range. However, this does not alter the optimal design of the fixed-bed reactor, aside from the fact that more tubes are necessary to convert the maximum load. For the maximum load, the operating parameters are identical to the *base case*. For loads lower than the maximum load, the operating parameters are chosen such that the carbon dioxide conversion is kept above 95%. However, there is no significant potential to compensate for the increasing number of tubes, which rises linearly with the maximum load. Since reactor volume, which is obtained by the increased number of tubes, is redundant for lower loads, the mean methane space–time yield behaves almost inversely proportional to the load range, as seen in Fig. 5.

Step response analyses between the optimal steady states revealed an unfavorable dynamic behavior of reactors with diluted catalyst beds. Especially for the cases with two and infinite bed segments, traveling hot-spots with temperatures far above the maximum steady-state temperature were observed. The same holds for reactors filled with core–shell catalyst particles with infinite segments due to the section with pure, uniform catalyst particles at the inlet. In these cases, the transition between steady states has to be done more carefully, e.g., by ramping the operating parameters. Another possibility is the consideration of runaway criteria in transient scenarios or dynamic optimization (see e.g., [20,21,55]). On the contrary, the reactors filled with core–shell catalyst particles with one and two fixed-bed segments did not show any unfavorable dynamic behavior (e.g., moving reaction fronts). After a load change, the new steady state settles quickly, and no pronounced temperature excursions are observed.

Based on the results of this study, a fixed-bed reactor filled uniformly with core–shell catalyst particles appears as a promising candidate for load-flexible methanation reactors, as it offers comparably high methane space–time yields and is able to deal with drastic loads changes without showing any unfavorable dynamic behavior. If higher space–time yields are required, two fixed-bed segments, of which only the first consists of core–shell catalyst particles, can be considered. However, this also requires a more complex operation strategy. In a broader sense, the inert shell on the catalyst particles can be interpreted as spatially optimized placement of the inert material considering reactor and particle scale in comparison to ordinary fixed-bed dilution.

Additionally, assuming uniform producibility of core–shell catalyst particles, a fixed-bed consisting of such particles is not inherently prone to statistical activity variations, as it is the case for highly diluted fixed-beds [56].

7. List of symbols

Latin symbols

A_w	Parameter in Eq. (12) (–)
B_w	Parameter in Eq. (12) (–)
Bi	Biot number (–)
c_p	Isobaric heat capacity $\left(\frac{J}{kg\ K}\right)$
c	Concentration $\left(\frac{mol}{m^3}\right)$
d	Particle diameter (m)
D	Tube diameter (m)
DoF	Degrees of freedom (var. unit)
$\mathfrak{D}$	Diffusion coefficient $\left(\frac{m^2}{s}\right)$
H	Enthalpy $\left(\frac{J}{mol}\right)$
k	Reaction rate constant $\left(\frac{mol}{Pa\ kg\ s}\right)$
K	Adsorption constant (var. unit)
L	Load $\left(\frac{kg}{s}\right)$
ΔL	Load range $\left(\frac{kg}{s}\right)$
$\bar{L}$	Mean load $\left(\frac{kg}{s}\right)$
$\mathfrak{L}$	Reactor length (m)
M	Molar mass $\left(\frac{kg}{mol}\right)$
$\dot{n}$	Molar flux $\left(\frac{mol}{m^2\ s}\right)$
n	Catalyst geometry factor (–)
N	Number of loads (–)
N_T	Number of tubes (–)
p	Pressure (Pa)
Pe	Peclet number (–)
r	Radial catalyst particle coordinate (m)
R	Radius (m)
R_{gas}	Ideal gas constant $\left(\frac{J}{mol\ K}\right)$
S	Selectivity (–)
STY	Space–time yield $\left(\frac{kg}{m^3\ s}\right)$
t	Time (s)
T	Temperature (K)
u	Superficial gas velocity $\left(\frac{m}{s}\right)$
U	Overall heat transfer coeff. $\left(\frac{W}{m^2\ K}\right)$
U'	Overall heat transfer coeff. $\left(\frac{W}{m^2\ K}\right)$
V	Volume (m^3)
X	Carbon dioxide conversion (–)
z	Axial reactor coordinate (m)

Greek symbols

α	Heat transfer coefficient $\left(\frac{W}{m^2\ K}\right)$ -
β	Mass transfer coefficient $\left(\frac{m}{s}\right)$
γ	Heat conductivity ratio (–)
δ	diml. shell thickness (–)
ϵ	Void fraction (–)
ζ	Catalyst particle fraction (–)
η	Catalyst effectiveness factor (–)
Θ	Volume ratio (–)
κ	Parameter in Eq. (22) (–)
λ	Heat conductivity $\left(\frac{W}{m\ K}\right)$
Λ	Eff. heat conductivity $\left(\frac{W}{m\ K}\right)$
μ	Dynamic viscosity (Pa s)
ν	Stoichiometric coefficient (–)
ξ	Switched parameter in Eq. (22)
ρ	Density $\left(\frac{kg}{m^3}\right)$
σ	Reaction rate $\left(\frac{mol}{m^3\ s}\right)$
τ	Tortuosity (–)
Φ	Modified Thiele-Modulus (–)
Ψ	Defined by Eq. (32) (var. unit)
Ω	Defined by Eq. (31) $\left(\frac{1}{m}\right)$

Indices

$\square_i$	Comp. $i \in \{CO_2, H_2, CH_4, H_2O, CO\}$
$\square_j$	Load $j \in \{1, .., N\}$
$\square_k$	Reaction $k \in \{CO_2$ methanation, CO methanation, reverse water gas shift reaction$\}$
$\square_{CH_4}$	Methane
$\square_{CO_2}$	Carbon dioxide
$\square_{CO}$	Carbon monoxide
$\square_{H_2}$	Hydrogen
$\square_{H_2O}$	Water
$\square_{ax}$	Axial
$\square_{bed}$	Fixed-bed
$\square_{bulk}$	Gas phase bulk
$\square_{in}$	Inlet
$\square_{cool}$	Coolant
$\square_{core}$	Catalyst particle core
$\square_c$	Reactor tube center
$\square_{eff}$	Effective
$\square_{fluid}$	Fluid
$\square_{solid}$	Non-porous solid
$\square_{shell}$	Catalyst particle shell
$\square_r$	Radial
$\square_R$	Reactor
$\square_{switch}$	Switching position
$\square_{max}$	Maximum
$\square_M$	Molar
$\square_w$	Wall
$\square_{in}$	Inside
$\square_{int}$	Intrinsic
$\square_{out}$	Outside
$\square_0$	At initial time

Declaration of competing interest

The authors declare that they have no known competing financial interests or personal relationships that could have appeared to influence the work reported in this paper.

Acknowledgments

This research work was conducted within the DFG Priority Program SPP2080 "Catalysts and reactors under dynamic conditions for energy storage and conversion" and was funded by the Deutsche Forschungsgemeinschaft (DFG, German Research Foundation) -406914011. Ronny Zimmermann and Jens Bremer are also affiliated with the International Max Planck Research School (IMPRS) for Advanced Methods in Process and Systems Engineering, Magdeburg, Germany. (Gefördert durch die Deutsche Forschungsgemeinschaft (DFG)-406914011.)

Appendix A. Influence of the reverse water gas shift reaction

To study the assumption of negligible CO formation in core–shell catalyst particles, the mass balance equations

$$\frac{1}{r^n}\frac{\mathrm{d}}{\mathrm{d}r}\left[r^n \mathfrak{D}_{i,\mathrm{core}}\frac{\mathrm{d}c_{i,\mathrm{core}}}{\mathrm{d}r}\right] = \sum_k \nu_{i,k}\sigma_{k,\mathrm{core}}, \tag{24}$$

$$\frac{1}{r^n}\frac{\mathrm{d}}{\mathrm{d}r}\left[r^n \mathfrak{D}_{i,\mathrm{shell}}\frac{\mathrm{d}c_{i,\mathrm{shell}}}{\mathrm{d}r}\right] = 0, \tag{25}$$

$$\mathfrak{D}_{i,\mathrm{core}}\left.\frac{\mathrm{d}c_{i,\mathrm{core}}}{\mathrm{d}r}\right|_{r=0} = 0, \tag{26}$$

$$c_{i,\mathrm{core}}|_{r=R_{\mathrm{core}}} = c_{i,\mathrm{shell}}|_{r=R_{\mathrm{core}}}, \tag{27}$$

$$\mathfrak{D}_{i,\mathrm{core}}\left.\frac{\mathrm{d}c_{i,\mathrm{core}}}{\mathrm{d}r}\right|_{r=R_{\mathrm{core}}} = \mathfrak{D}_{i,\mathrm{shell}}\left.\frac{\mathrm{d}c_{i,\mathrm{shell}}}{\mathrm{d}r}\right|_{r=R_{\mathrm{core}}}, \tag{28}$$

$$\mathfrak{D}_{i,\mathrm{shell}}\left.\frac{\mathrm{d}c_{i,\mathrm{shell}}}{\mathrm{d}r}\right|_{r=R_{\mathrm{shell}}} = \beta_i\left(c_{i,\mathrm{bulk}} - c_{i,\mathrm{shell}}\right) \tag{29}$$

are solved for the species CO_2, H_2, CH_4, CO and H_2O and in addition to the CO_2 methanation the reverse water gas shift reaction and the CO methanation reaction

$$CO_2 + H_2 \rightleftharpoons CO + H_2O$$
$$CO + 3H_2 \rightleftharpoons CH_4 + H_2O$$

are included. The reaction kinetic model of Burger et al. [57], which is derived for the same catalyst as that of Koschany et al. [40], and model 11 of Lalinde et al. [58] are employed. For the latter, a 30 wt-% NiO/Al_2O_3 catalyst was used. The equation system is solved numerically at the optimal conditions of case 2a given in Section 5 at $X = 0\%$. Additionally, the results are compared to an uniform catalyst particle.

As displayed in Fig. 9, the methane selectivity of the catalyst of Koschany et al. [40] and Burger et al. [57] is above 95%, regardless of whether core–shell particles or uniform catalyst particles are used. However, for the catalyst of Lalinde et al. [58], the selectivity decreases significantly with rising temperatures in the case of uniform catalyst particles. When core–shell catalyst particles are employed, the selectivity towards methane remains high. The reason for this is a hydrogen surplus inside the catalyst particles, which is caused by the high effective diffusion coefficient of hydrogen compared to the other reactants. Thus, the chemical equilibrium is shifted from carbon monoxide towards methane inside the catalyst particles. Additionally, the target product methane exhibits a higher effective diffusion coefficient than carbon monoxide and consequently diffuses quicker out of the porous core and through the inert shell.

Appendix B. Catalyst effectiveness factor approximation

To derive the catalyst effectiveness factor $\eta = \sigma_{\mathrm{eff}}/\sigma_{\mathrm{int}}$, the catalyst mass balance Eqs. (24)–(29) have to be solved for the concentration profiles. If only a single reaction takes place, it is sufficient to consider the catalyst pellet mass balance equations of a single component. The concentration profiles of the remaining components can then be obtained from the stoichiometric relations [59]. Therefore, the index i is omitted in the following. In general, no analytical solution for arbitrary reaction kinetic expressions can be given. However, it is possible to derive solutions at the limit of low and high reaction rates.

Solution in the regime of low reaction rates

The solution at the limit of low reaction rate can be obtained straight forward, as the concentrations in the catalyst particle are the same as the concentrations in the gas phase. In consequence, also the reaction rates are everywhere the same.

$$\eta = \frac{\int_0^{R_{\mathrm{shell}}}\sigma r^n \mathrm{d}r}{\int_0^{R_{\mathrm{shell}}}\sigma_{\mathrm{bulk}} r^n \mathrm{d}r} = \frac{\int_0^{R_{\mathrm{core}}} r^n \mathrm{d}r}{\int_0^{R_{\mathrm{shell}}} r^n \mathrm{d}r} = \frac{1}{(1+\delta)^{n+1}} \tag{30}$$

In this case, the influence of the inert shell reduces to a mere dilution factor with $\delta = \frac{R_{\mathrm{shell}} - R_{\mathrm{core}}}{R_{\mathrm{core}}}$.

Solution in the regime of high reaction rates

For the solution at the limit of high reactions rates, the mass balance equation of the shell together with the boundary conditions are solved at first [60]:

$$\left.\frac{\mathrm{d}c_{\mathrm{core}}}{\mathrm{d}r}\right|_{r=R_{\mathrm{core}}} = \frac{(c_{\mathrm{bulk}} - c_{\mathrm{core}}(R_{\mathrm{core}}))}{\frac{\mathfrak{D}_{\mathrm{core}}}{\beta}\frac{R_{\mathrm{core}}^n}{R_{\mathrm{shell}}^n} + \frac{\mathfrak{D}_{\mathrm{core}}R_{\mathrm{core}}^n\Psi}{\mathfrak{D}_{\mathrm{shell}}}} = \Omega(c_{\mathrm{bulk}} - c_{\mathrm{core}}(R_{\mathrm{core}})). \tag{31}$$

with Ψ as function of the particle geometry:

$$\int_{R_{\mathrm{core}}}^{R_{\mathrm{shell}}}\frac{\mathrm{d}r}{r^n} = \Psi(n, R_{\mathrm{core}}, R_{\mathrm{shell}}). \tag{32}$$

If the reaction rate in the catalyst particle core is sufficiently high, the reaction essentially takes place in a thin layer at the boundary between shell and core. In this case, the mass balance of the core can be simplified to:

$$\frac{1}{r^n}\frac{\mathrm{d}}{\mathrm{d}r}\left[r^n\mathfrak{D}_{\mathrm{core}}\frac{\mathrm{d}c_{\mathrm{core}}}{\mathrm{d}r}\right] \approx \mathfrak{D}_{\mathrm{core}}\frac{\mathrm{d}}{\mathrm{d}r}\left[\frac{\mathrm{d}c_{\mathrm{core}}}{\mathrm{d}r}\right] = \sigma(c_{\mathrm{core}}). \tag{33}$$

This equation can be solved to obtain [61]:

$$\left.\frac{\mathrm{d}c_{\mathrm{core}}}{\mathrm{d}r}\right|_{r=R_{\mathrm{core}}} = F - \frac{\sigma(c_{\mathrm{bulk}})}{\mathfrak{D}_{\mathrm{core}}F}(c_{\mathrm{bulk}} - c_{\mathrm{core}}(R_{\mathrm{core}})). \tag{34}$$

with $F = \sqrt{\frac{2}{\mathfrak{D}_{\mathrm{core}}}\int_{c_{\mathrm{eq}}}^{c_{\mathrm{bulk}}}\sigma(c_{\mathrm{core}})\mathrm{d}c}$.

Eqs. (31) and (34) are set equal to calculate the concentration at the boundary between shell and core:

$$(c_{\mathrm{bulk}} - c_{\mathrm{core}}(R_{\mathrm{core}})) = \frac{1}{\frac{\Omega}{F} + \frac{\sigma(c_{\mathrm{bulk}})}{\mathfrak{D}_{\mathrm{core}}F^2}}. \tag{35}$$

With this information, the effectiveness factor at the limit of very high reaction rates can be calculated as

$$\eta = \frac{(n+1)R_{\mathrm{core}}^n}{R_{\mathrm{shell}}^{n+1}}\left[\frac{\sigma_{\mathrm{bulk}}}{\mathfrak{D}_{\mathrm{core}}F} + \frac{\mathfrak{D}_{\mathrm{core}}}{\beta\mathfrak{D}_{\mathrm{core}}^2}\frac{R_{\mathrm{core}}^n}{R_{\mathrm{shell}}^n}\frac{\sigma_{\mathrm{bulk}}^2}{F^2} + \frac{\mathfrak{D}_{\mathrm{core}}R_{\mathrm{core}}^n\Psi}{\mathfrak{D}_{\mathrm{shell}}\mathfrak{D}_{\mathrm{core}}^2}\frac{\sigma_{\mathrm{bulk}}^2}{F^2}\right]^{-1} \tag{36}$$

or in dimensionless form as

$$\frac{1}{\eta} = (1+\delta)^{n+1}\left[\Phi + \frac{\Phi^2}{\mathrm{Bi}_{\mathrm{ext}}(1+\delta)^n} + \frac{\Phi^2}{\mathrm{Bi}_{\mathrm{int}}}\right] \tag{37}$$

$$\text{with}\quad \Phi = \frac{R_{\mathrm{core}}\sigma_{\mathrm{bulk}}}{\mathfrak{D}_{\mathrm{core}}F(n+1)},\quad \mathrm{Bi}_{\mathrm{ext}} = \frac{\beta R_{\mathrm{core}}}{\mathfrak{D}_{\mathrm{core}}(n+1)},\quad \mathrm{Bi}_{\mathrm{int}} = \frac{\mathfrak{D}_{\mathrm{shell}}}{\mathfrak{D}_{\mathrm{core}}R_{\mathrm{core}}^{n-1}\Psi(n+1)}. \tag{38}$$

Interpolation of both regimes

Both regimes can be interpolated, to obtain an equation, which serves as an approximation over the whole range of reaction rates.

$$\frac{1}{\eta} = (1+\delta)^{n+1}\left[\frac{\Phi}{\tanh(\Phi)} + \frac{\Phi^2}{\mathrm{Bi}_{\mathrm{ext}}(1+\delta)^n} + \frac{\Phi^2}{\mathrm{Bi}_{\mathrm{int}}}\right] \tag{39}$$

It has to be noted, that the degree of approximation obtained in the interpolated regime is fortuitous and has to be checked before application. Especially, as no multiple steady states can be described by this method. However, the approximation is sufficient for many engineering problems.

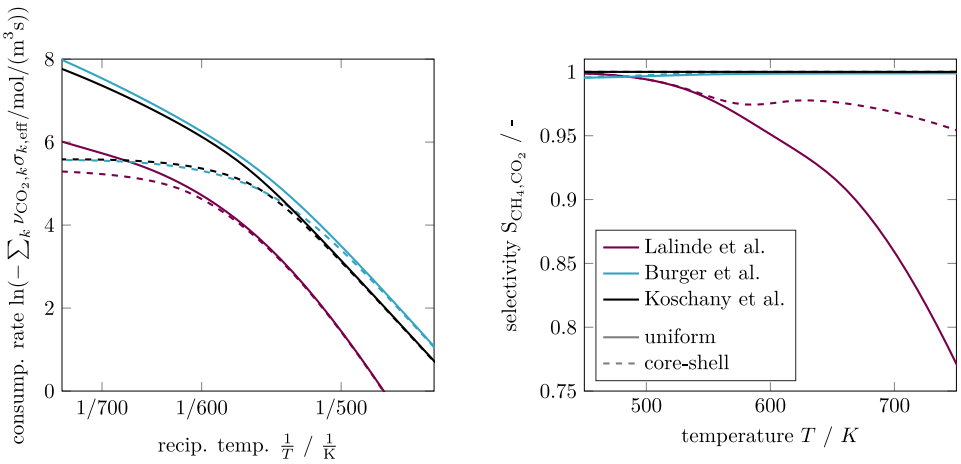

Fig. 9. Arrhenius plots of the carbon dioxide consumption rate (left) and methane selectivity (right) of uniform and core–shell catalyst particles for various reaction kinetic models. Parameters of the particles are chosen according to the optimal results in Section 5.

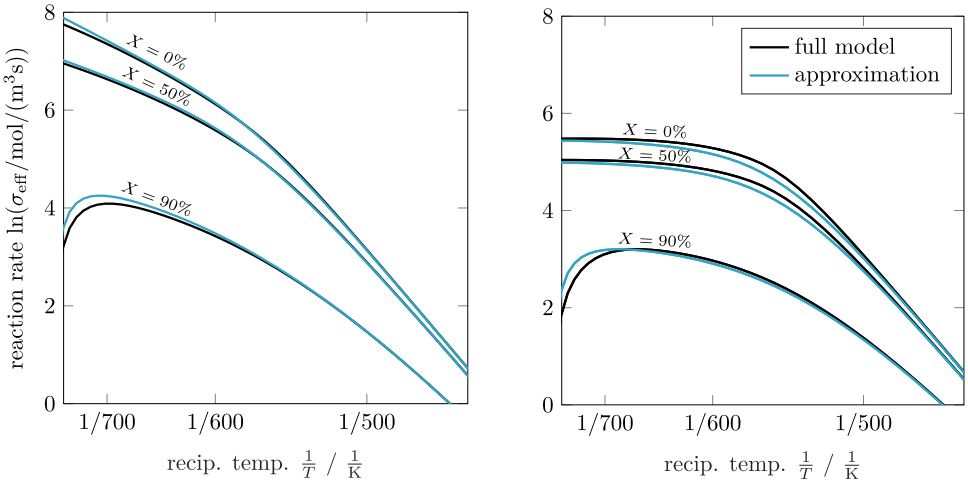

Fig. 10. Arrhenius plots of uniformly active (left) and core–shell catalyst particles (right) at different carbon dioxide conversions (0%, 50%, 90%). Parameters of the particles are chosen according to the optimal results in Section 5.

Practical application

In practical applications, two problems arise when calculating the Thiele modulus Φ in Eq. (37). First, reactions kinetic models are often too complex and the integral cannot be evaluated. Therefore, another approach is to evaluate the integral according to the Trapezoidal rule:

$$\int_{c_{\mathrm{eq}}}^{c_{\mathrm{bulk}}} \sigma(c_{\mathrm{core}})\mathrm{d}c \approx (c_{\mathrm{bulk}} - c_{\mathrm{eq}})\frac{\sigma(c_{\mathrm{bulk}}) - \sigma(c_{\mathrm{eq}})}{2} = (c_{\mathrm{bulk}} - c_{\mathrm{eq}})\frac{\sigma(c_{\mathrm{bulk}})}{2}. \tag{40}$$

The second problem is that for equilibrium reactions, the equilibrium concentration in the particle core is not known. This can be dealt with by assuming it equal to the equilibrium concentration in the bulk. Now, the Thiele-modulus can be expressed as:

$$\Phi = \frac{R_{\mathrm{core}}}{n+1}\sqrt{\frac{\sigma(c_{\mathrm{bulk}})}{\mathfrak{D}_{\mathrm{core}}(c_{\mathrm{bulk}} - c_{\mathrm{eq,bulk}})}}. \tag{41}$$

Comparison to rigorously solved catalyst particle mass balance equations

The applicability of the derived solution for the reaction kinetic model of Koschany et al. [40] for the methanation of carbon dioxide is studied by comparing the effective reaction rates in the Arrhenius plot to the rigorous solution of Eqs. (24)–(29). For this purpose, the approximation (Eq. (37)) is evaluated with respect to carbon dioxide. Fig. 10 displays the Arrhenius plot for a uniformly active catalyst particle and a core–shell catalyst particle at different carbon dioxide conversions of a stoichiometric and undiluted mixture of carbon dioxide and hydrogen. The approximation is able to describe the effective reaction rate calculated with the rigorous model to a sufficient degree but requires only a fraction of the computational effort and is fully explicit.

References

[1] S. Rönsch, J. Schneider, S. Matthischke, M. Schlüter, M. Götz, J. Lefebvre, P. Prabhakaran, S. Bajohr, Review on methanation – From fundamentals to current projects, Fuel 166 (2016) 276–296, http://dx.doi.org/10.1016/j.fuel.2015.10.111.

[2] A. Kummer, T. Varga, Completion of thermal runaway criteria: Two new criteria to define runaway limits, Chem. Eng. Sci. 196 (2019) 277–290, http://dx.doi.org/10.1016/j.ces.2018.11.008.

[3] K.F. Kalz, R. Kraehnert, M. Dvoyashkin, R. Dittmeyer, R. Gläser, U. Krewer, K. Reuter, J.-D. Grunwaldt, Future challenges in heterogeneous catalysis: Understanding catalysts under dynamic reaction conditions, ChemCatChem 9 (1) (2017) 17–29, http://dx.doi.org/10.1002/cctc.201600996.

[4] J. Riese, M. Grünewald, Challenges and opportunities to enhance flexibility in design and operation of chemical processes, Chem. Ing. Tech. 92 (12) (2020) 1887–1897, http://dx.doi.org/https://doi.org/10.1002/cite.202000057.

[5] S.M. Biollaz, T.J. Schildhauer (Eds.), Synthetic Natural Gas from Coal, Dry Biomass, and Power-to-Gas Applications, John Wiley & Sons Inc, Hoboken, New Jersey, 2016.

[6] S. Matthischke, R. Krüger, S. Rönsch, R. Güttel, Unsteady-state methanation of carbon dioxide in a fixed-bed recycle reactor — Experimental results for transient flow rate ramps, Fuel Process. Technol. 153 (2016) 87–93, http://dx.doi.org/10.1016/j.fuproc.2016.07.021.

[7] S. Theurich, S. Rönsch, R. Güttel, Transient flow rate ramps for methanation of carbon dioxide in an adiabatic fixed-bed recycle reactor, Energy Technol. 8 (3) (2020) 1901116, http://dx.doi.org/https://doi.org/10.1002/ente.201901116.

[8] R. van Basshuysen, Erdgas und erneuerbares Methan für den Fahrzeugantrieb, Springer Fachmedien Wiesbaden, Wiesbaden, 2015, http://dx.doi.org/10.1007/978-3-658-07159-2.

[9] H. Harms, B. Höhlein, A. Skov, Methanisierung kohlenmonoxidreicher Gase beim Energie-Transport, Chem. Ing. Tech. 52 (6) (1980) 504–515, http://dx.doi.org/10.1002/cite.330520605.

[10] B. Kreitz, G.D. Wehinger, T. Turek, Dynamic simulation of the CO_2 methanation in a micro-structured fixed-bed reactor, Chem. Eng. Sci. 195 (2019) 541–552, http://dx.doi.org/https://doi.org/10.1016/j.ces.2018.09.053.

[11] L. Kiewidt, Solid sponges as support for heterogeneous catalysts in gas-phase reactions (Dissertation) Universität Bremen. URL http://d-nb.info/1150833947/34.

[12] D. Schlereth, O. Hinrichsen, A fixed-bed reactor modeling study on the methanation of CO_2, Chem. Eng. Res. Des. 92 (4) (2014) 702–712, http://dx.doi.org/10.1016/j.cherd.2013.11.014.

[13] A. El Sibai, L.K. Rihko Struckmann, K. Sundmacher, Model-based optimal Sabatier reactor design for power-to-gas applications, Energy Technol. 5 (6) (2017) 911–921, http://dx.doi.org/10.1002/ente.201600600.

[14] J. Bremer, K. Sundmacher, Operation range extension via hot-spot control for catalytic CO_2 methanation reactors, React. Chem. Eng. 4 (6) (2019) 1019–1037, http://dx.doi.org/10.1039/C9RE00147F.

[15] G.F. Froment, Fixed bed catalytic reactors—Current design status, Ind. Eng. Chem. 59 (2) (1967) 18–27, http://dx.doi.org/10.1021/ie50686a006.

[16] J.S. Buchanan, S. Sundaresan, Optimal catalyst distribution and dilution in nonisothermal packed bed reactors, Chem. Eng. Commun. 52 (1–3) (1987) 33–51, http://dx.doi.org/10.1080/00986448708911856.

[17] W.L. Luyben, Catalyst dilution to improve dynamic controllability of cooled tubular reactors, Comput. Chem. Eng. 37 (2012) 184–190, http://dx.doi.org/10.1016/j.compchemeng.2011.07.017.

[18] Y. Nie, P.M. Witt, A. Agarwal, L.T. Biegler, Optimal active catalyst and inert distribution in catalytic packed bed reactors: ortho-xylene oxidation, Ind. Eng. Chem. Res. 52 (44) (2013) 15311–15320, http://dx.doi.org/10.1021/ie4005699.

[19] M.M. Quina, R.M. Quinta-Ferreira, Start-up and wrong-way behavior in a tubular reactor: dilution effect of the catalytic bed, Chem. Eng. Sci. 55 (18) (2000) 3885–3897, http://dx.doi.org/10.1016/S0009-2509(00)00029-4.

[20] A. Fache, F. Marias, V. Guerré, S. Palmade, Optimization of fixed-bed methanation reactors: Safe and efficient operation under transient and steady-state conditions, Chem. Eng. Sci. 192 (2018) 1124–1137, http://dx.doi.org/10.1016/j.ces.2018.08.044.

[21] K.L. Fischer, H. Freund, Intensification of load flexible fixed bed reactors by optimal design of staged reactor setups, Chem. Eng. Process.: Process Intensif. (2020) 108183, http://dx.doi.org/10.1016/j.cep.2020.108183.

[22] K.L. Fischer, H. Freund, On the optimal design of load flexible fixed bed reactors: Integration of dynamics into the design problem, Chem. Eng. J. 393 (2020) 124722, http://dx.doi.org/10.1016/j.cej.2020.124722.

[23] S.K. Mazidi, M.T. Sadeghi, M.A. Marvast, Optimization of Fischer-Tropsch process in a fixed-bed reactor using non-uniform catalysts, Chem. Eng. Technol. 36 (1) (2013) 62–72, http://dx.doi.org/10.1002/ceat.201200268.

[24] R. Baratti, A. Gavriilidis, M. Morbidelli, A. Varma, Optimization of a nonisothermal nonadiabatic fixed-bed reactor using dirac-type silver catalysts for ethylene epoxidation, Chem. Eng. Sci. 49 (12) (1994) 1925–1936, http://dx.doi.org/10.1016/0009-2509(94)80077-4.

[25] R.T. Zimmermann, J. Bremer, K. Sundmacher, Optimal catalyst particle design for flexible fixed-bed CO_2 methanation reactors, Chem. Eng. J. 387 (2020) 123704, http://dx.doi.org/10.1016/j.cej.2019.123704.

[26] I.E. Grossmann, R.W.H. Sargent, Optimum design of multipurpose chemical plants, Ind. Eng. Chem. Process Des. Dev. 18 (2) (1979) 343–348, http://dx.doi.org/10.1021/i260070a031.

[27] D.K. Varvarezos, I.E. Grossmann, L.T. Biegler, An outer-approximation method for multiperiod design optimization, Ind. Eng. Chem. Res. 31 (6) (1992) 1466–1477, http://dx.doi.org/https://doi.org/10.1021/ie00006a008.

[28] L.T. Biegler, I.E. Grossmann, Retrospective on optimization, Comput. Chem. Eng. 28 (8) (2004) 1169–1192, http://dx.doi.org/https://doi.org/10.1016/j.compchemeng.2003.11.003.

[29] K.L. Fischer, M.R. Langer, H. Freund, Dynamic carbon dioxide methanation in a wall-cooled fixed bed reactor: Comparative evaluation of reactor models, Ind. Eng. Chem. Res. (2019) http://dx.doi.org/https://doi.org/10.1021/acs.iecr.9b02863.

[30] G. Eigenberger, On the dynamic behavior of the catalytic fixed-bed reactor in the region of multiple steady states—I. The influence of heat conduction in two phase models, Chem. Eng. Sci. 27 (11) (1972) 1909–1915, http://dx.doi.org/10.1016/0009-2509(72)87049-0.

[31] V. Pinjala, Y.C. Chen, D. Luss, Wrong-way behavior of packed-bed reactors: II. Impact of thermal dispersion, AIChE J. 34 (10) (1988) 1663–1672, http://dx.doi.org/10.1002/aic.690341010.

[32] J. Bremer, K. Sundmacher, Novel uniqueness and multiplicity criteria for non-isothermal fixed-bed reactors, exemplified for catalytic CO_2 methanation, Front. Energy Res. 8 (2020) 549298, http://dx.doi.org/https://doi.org/10.3389/fenrg.2020.549298.

[33] A.G. Dixon, An improved equation for the overall heat transfer coefficient in packed beds, Chem. Eng. Process.: Process Intensif. 35 (5) (1996) 323–331, http://dx.doi.org/10.1016/0255-2701(96)80012-2.

[34] S. Yagi, D. Kunii, Studies on effective thermal conductivities in packed beds, AIChE J. 3 (3) (1957) 373–381, http://dx.doi.org/10.1002/aic.690030317.

[35] H. Martin, M. Nilles, Radiale Wärmeleitung in durchströmten Schüttungsrohren, Chem. Ing. Tech. 65 (12) (1993) 1468–1477, http://dx.doi.org/10.1002/cite.330651206.

[36] E. Tsotsas, H. Martin, Thermal conductivity of packed beds: A review, Chem. Eng. Process.: Process Intensif. 22 (1) (1987) 19–37, http://dx.doi.org/10.1016/0255-2701(87)80025-9.

[37] VDI Heat Atlas, second ed., Springer-Verlag Berlin Heidelberg, Berlin, ISBN: 978-3-540-79999-3, 2010, http://dx.doi.org/https://doi.org/10.1007/978-3-540-77877-6.

[38] B. Eisfeld, K. Schnitzlein, The influence of confining walls on the pressure drop in packed beds, Chem. Eng. Sci. 56 (14) (2001) 4321–4329, http://dx.doi.org/10.1016/S0009-2509(00)00533-9.

[39] B.E. Poling, J.M. Prausnitz, J.P. O'Connell, The Properties of Gases and Liquids, in: McGraw Hill professional, McGraw-Hill Professional, New York, ISBN: 0-07-011682-2, 2001.

[40] F. Koschany, D. Schlereth, O. Hinrichsen, On the kinetics of the methanation of carbon dioxide on coprecipitated $NiAl(O)_x$, Appl. Catal. B 181 (2016) 504–516, http://dx.doi.org/10.1016/j.apcatb.2015.07.026.

[41] J. Bremer, K.H.G. Rätze, K. Sundmacher, CO_2 methanation: Optimal start-up control of a fixed-bed reactor for power-to-gas applications, AIChE J. 63 (1) (2017) 23–31, http://dx.doi.org/10.1002/aic.15496.

[42] P. Harriott, Thermal conductivity of catalyst pellets and other porous particles, Chem. Eng. J. 10 (1) (1975) 65–71, http://dx.doi.org/10.1016/0300-9467(75)88018-X.

[43] N. Wakao, T. Funazkri, Effect of fluid dispersion coefficients on particle-to-fluid mass transfer coefficients in packed beds, Chem. Eng. Sci. 33 (10) (1978) 1375–1384, http://dx.doi.org/10.1016/0009-2509(78)85120-3.

[44] B. Tjaden, S.J. Cooper, D.J.L. Brett, D. Kramer, P.R. Shearing, On the origin and application of the Bruggeman correlation for analysing transport phenomena in electrochemical systems, Curr. Opin. Chem. Eng. 12 (2016) 44–51, http://dx.doi.org/https://doi.org/10.1016/j.coche.2016.02.006.

[45] S. Torquato, Random Heterogeneous Materials: Microstructure and Macroscopic Properties, in: Interdisciplinary Applied Mathematics, vol. 16, Springer, New York, NY, 2002, http://dx.doi.org/10.1007/978-1-4757-6355-3.

[46] VDI-Wärmeatlas: Mit 320 Tabellen, eleventh ed., in: VDI-Buch, Springer Vieweg, Berlin, 2013, http://dx.doi.org/10.1007/978-3-642-19981-3.

[47] E.L. Oliveira, C.A. Grande, A.E. Rodrigues, Methane steam reforming in large pore catalyst, Chem. Eng. Sci. 65 (5) (2010) 1539–1550, http://dx.doi.org/10.1016/j.ces.2009.10.018.

[48] J. Ducamp, A. Bengaouer, P. Baurens, Modelling and experimental validation of a CO_2 methanation annular cooled fixed-bed reactor exchanger, Can. J. Chem. Eng. 95 (2) (2017) 241–252, http://dx.doi.org/10.1002/cjce.22706.

[49] J. Andersson, A General-Purpose Software Framework for Dynamic Optimization (Ph.D. thesis), Arenberg Doctoral School, KU Leuven, Department of Electrical Engineering (ESAT/SCD) and Optimization in Engineering Center, Kasteelpark Arenberg 10, 3001-Heverlee, Belgium, 2013.

[50] J.A.E. Andersson, J. Gillis, G. Horn, J.B. Rawlings, M. Diehl, CasADi: a software framework for nonlinear optimization and optimal control, Math. Program. Comput. 11 (1) (2019) 1–36, http://dx.doi.org/10.1007/s12532-018-0139-4.

[51] A.C. Hindmarsh, P.N. Brown, K.E. Grant, S.L. Lee, R. Serban, D.E. Shumaker, C.S. Woodward, SUNDIALS: Suite of nonlinear and differential/algebraic equation solvers, ACM Trans. Math. Softw. 31 (3) (2005) 363–396.

[52] A. Wächter, L.T. Biegler, On the implementation of an interior-point filter line-search algorithm for large-scale nonlinear programming, Math. Program. 106 (1) (2006) 25–57, http://dx.doi.org/10.1007/s10107-004-0559-y.

[53] HSL, A collection of Fortran codes for large-scale scientific computation, 2007.

[54] A. Fache, F. Marias, Dynamic operation of fixed-bed methanation reactors: Yield control by catalyst dilution profile and magnetic induction, Renew. Energy 151 (2020) 865–886, http://dx.doi.org/10.1016/j.renene.2019.11.081.

[55] J. Bremer, P. Goyal, L. Feng, P. Benner, K. Sundmacher, Nonlinear model order reduction for catalytic tubular reactors, in: 26th European Symposium on Computer Aided Process Engineering, in: Computer Aided Chemical Engineering, vol. 38, Elsevier, 2016, pp. 2373–2378, http://dx.doi.org/10.1016/B978-0-444-63428-3.50400-8.

[56] G. Ganzer, H. Freund, Influence of statistical activity variations in diluted catalyst beds on the thermal reactor behavior: Derivation of an a priori criterion, Chem. Eng. Sci. 220 (2020) 115607, http://dx.doi.org/10.1016/j.ces.2020.115607.

[57] T. Burger, P. Donaubauer, O. Hinrichsen, On the kinetics of the co-methanation of CO and CO_2 on a co-precipitated Ni-Al catalyst, Appl. Catal. B 282 (2021) 119408, http://dx.doi.org/https://doi.org/10.1016/j.apcatb.2020.119408.

[58] J.A. Hernandez Lalinde, P. Roongruangsree, J. Ilsemann, M. Bäumer, J. Kopyscinski, CO_2 methanation and reverse water gas shift reaction. kinetic study based on in situ spatially-resolved measurements, Chem. Eng. J. 390 (2020) 124629, http://dx.doi.org/10.1016/j.cej.2020.124629.

[59] A. Burghardt, Transport phenomena and chemical reactions in porous catalysts for multicomponent and multireaction systems, Chem. Eng. Process.: Process Intensif. 20 (5) (1986) 229–244, http://dx.doi.org/10.1016/0255-2701(86)80016-2.

[60] M. Morbidelli, A. Varma, On shape normalization for non-uniformly active catalyst pellets—II, Chem. Eng. Sci. 38 (2) (1983) 297–305, http://dx.doi.org/10.1016/0009-2509(83)85012-X.

[61] R. Aris, The jail of shape, Chem. Eng. Commun. 24 (4–6) (1983) 167–181, http://dx.doi.org/10.1080/00986448308940080.